J Mater Sci (2008) 43:6353–6358
DOI 10.1007/s10853-008-2911-8

Effects of aerosol heating rate on the properties of aggregates of lead zirconate titanate nanoparticles produced by spray pyrolysis

Andrew J. Scott · William Nimmo · Ryan Scott · Andrew P. Brown · Steven J. Milne

Received: 4 January 2008 / Accepted: 28 July 2008 / Published online: 16 August 2008

Abstract The dependence of the shape and size distribution of aggregates of lead zirconate titanate nanoparticles prepared by spray pyrolysis of a sol–gel precursor solution is reported. Decreasing the average heating rate from 300 to 160 °C s^{-1} in the sub-200 °C section of the reactor decreased the proportion of non-spherical particle aggregates and decreased the maximum size from ~10 to ~5 μm. Microtome sectioning revealed an internal structure composed of <100 nm primary particles. Both solid and hollow particle aggregates were present.

Introduction

Spray pyrolysis (SP) offers a means of producing agglomerate-free powders, in which any chemical segregation is restricted to the dimensions of the droplets and the formed particles [1–6]. For lead zirconate titanate (PZT) powders, produced by twin-fluid-atomisation SP of a sol–gel precursor solution, we have previously demonstrated that the size and shape of the aggregates of nanoparticles are established during the initial, low-temperature drying stages [7, 8]. The product powders are mostly composed of spherical particles, but irregular partially collapsed particles are also present. The latter are postulated to derive from droplets which, on drying, form a gelatinous, pliable surface skin that subsequently collapses inward as solvent evaporates from the liquid trapped in the interior [7, 8]. This formation mechanism is in contrast to that of SP of metal-salt solutions, in which the surface layer is a brittle precipitated salt or hydroxide which usually fragments on further heating and solvent evaporation [1, 9]. Either type of hollow particle is thought to form due to an imbalance between the rates of solvent evaporation from the droplet surface and the rates of solute/solvent diffusion within the droplet. This leads to a solute concentration gradient in which the surface region exceeds the critical solute saturation concentration, and differential precipitation occurs. In order to form non-hollow particles it is desirable that conditions prevail such that precipitation or gelation occurs throughout the whole volume of the droplet.

We have observed that for PZT made by sol–gel SP the collapsed particles occur most frequently in the upper size fraction of the sample. This is thought to be because concentration gradients are potentially highest in the largest droplets of the aerosol, due to the longer diffusion distances. Moreover, the occurrence of premature surface gelation inhibits normal droplet shrinkage during drying, resulting in oversize particles.

Droplet size, solution concentration and solvent evaporation rate are therefore critical parameters as regards the formation of oversized, collapsed particles. We were already working near the limiting droplet size that can be achieved by twin-fluid nozzle atomisation (Sauter mean diameters ~10 μm, [10]), and reducing the concentration of the starting solution would have had an adverse effect on throughput. Therefore, in this paper we investigate the effects of changing the heating rates experienced by the aerosol droplets as they pass through the low-temperature, solvent evaporation stage of the reactor. Results are presented showing data for particle size and morphology of

A. J. Scott · R. Scott · A. P. Brown · S. J. Milne (✉)
Institute for Materials Research, University of Leeds, Leeds LS2 9JT, UK
e-mail: S.J.Milne@leeds.ac.uk

W. Nimmo
Energy and Resources Institute, University of Leeds, Leeds LS2 9JT, UK

aggregates of nanoparticles for two temperature profiles, corresponding to two different aerosol drying rates. Information is also provided on the internal structure of the particle aggregates.

Experimental procedure

Details of the precursor solution synthesis are provided elsewhere [7]. Briefly, solutions were prepared from lead acetate, zirconium acetate and titanium diisopropoxide bisacetylyacetonate in an acetic acid solution. The 2-m long SP reactor consisted of six heated sections, linked to provide three independently controllable temperature zones. The extent to which the rate of heating could be controlled in the early low-temperature stages of the reactor was constrained by the need to retain a sufficient remaining reactor length to allow the temperature to be increased to reach decomposition and crystallisation temperatures. This limited us to an approximately twofold increase in the length of the sub-200 °C section of the reactor, and a halving of the average heating rate. The new modified slow heating profile (for the critical low-temperature stage, ≤200 °C) produced an average heating rate of ~130 °C s^{-1} ('Profile S'), compared to ~200 °C s^{-1} for the faster drying profile ('Profile F') used in the previously published work [8]. The two temperature profiles are represented in Fig. 1. The total residence times were ~2.6 s, for both profiles. Particle size and shape were observed using a field emission gun SEM (Leo 1530 FEGSEM), and statistical data were obtained via digital image analysis (Carl Zeiss Vision, KS 400 Version 3 software). Four electron micrographs were analysed (magnification 5,000×) for samples of each heating rate. More than 500 particles, with a diameter >0.5 μm (this was consistent with the range of the light scattering analysis), were outlined manually for each sample making the results statistically relevant; overlapping particles were not selected. A graphic overlay of 2-D particle outlines was produced and converted to binary image files. Statistical information was generated on: particle count, particle area, particle dimensions ('diameter') and aspect ratio (FERET ratio). The latter is defined as the ratio of minimum to maximum 'diameters'.

Phase development was monitored using a Philips X-ray powder diffractometer (Cu Kα radiation). Particle sizing of the bulk powder samples was performed using a light scattering technique (Malvern Mastersizer) on 1 wt.% suspensions in a 0.1% Dispex A40 aqueous solution; the system was set-up to collect data from particles sized ≥0.5 μm.

Internal particle structure was revealed by microtoming particles embedded in epoxy resin (Reichert-Jung Ultracut E microtome). The sectioned particles were subsequently imaged using the SEM.

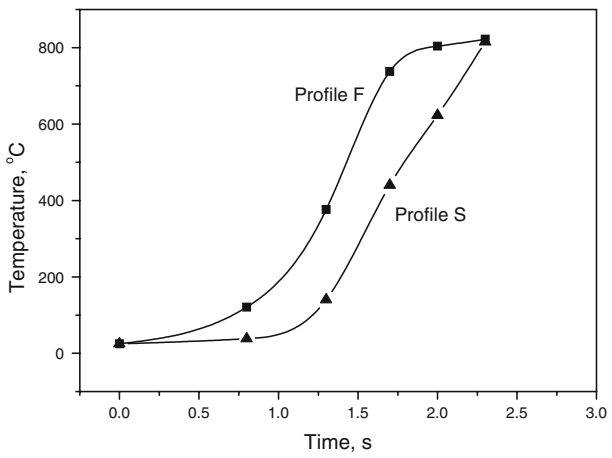

Fig. 1 Temperature–time profiles, F and S

Results

X-ray diffraction traces in Fig. 2 show PZT phase development in samples extracted from ports sited along the length of the reactor. A strong peak at ~29.5° 2θ and medium intensity peak at 34.2° 2θ indicate an intermediate pyrochlore crystallisation product, which co-exists with the desired perovskite phase at the temperatures of 600 to 700 °C (Fig. 2b, c). The perovskite phase is the dominant

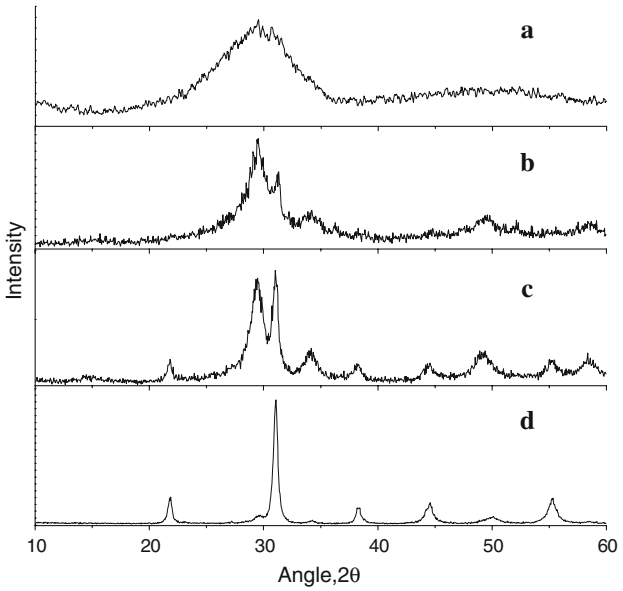

Fig. 2 PZT phase development (heating Profile S) showing reduction of the intermediate pyrochlore phase (peaks ~29.5° 2θ and 34.2° 2θ) with increasing temperature. Samples were extracted from the SP reactor at temperatures: (a) 350 °C, (b) 600 °C, (c) 700 °C, (d) 800 °C

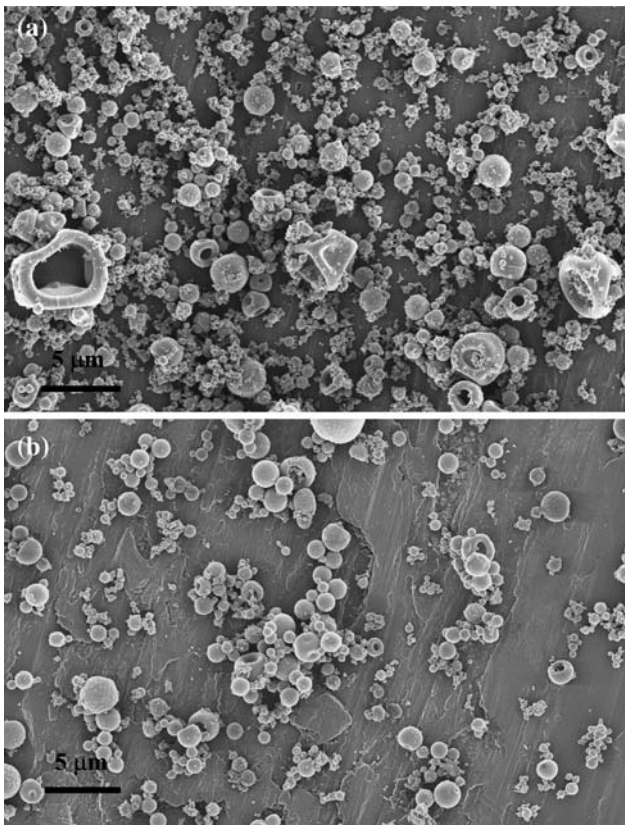

Fig. 3 Scanning electron micrograph showing particle size and morphology for (**a**) Profile F, (**b**) Profile S

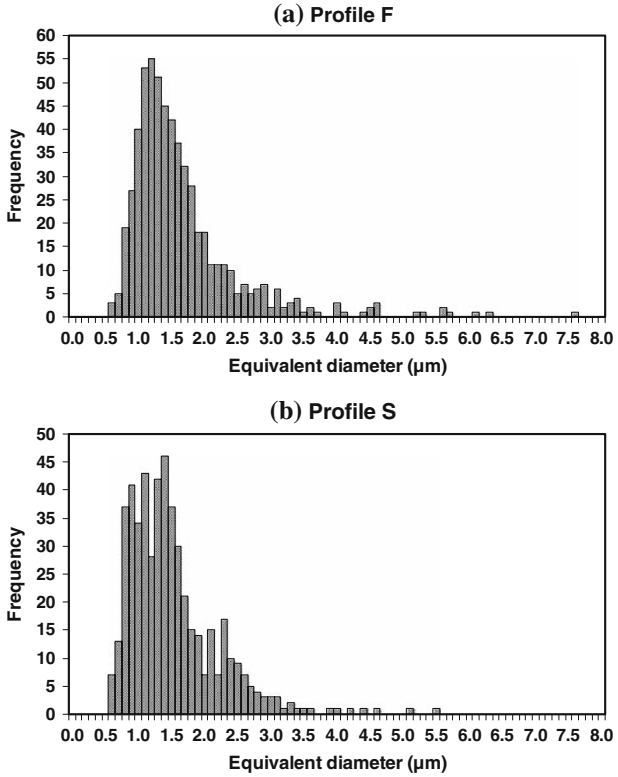

Fig. 4 Equivalent circular diameter particle size distributions for (**a**) Profile F and (**b**) Profile S

product in the 800 °C sample (Fig. 2d). Results for both heating profiles were similar.

Typical secondary electron images of the particle aggregates produced by both temperature profiles, and subsequently analysed for shape and size characteristics are shown in Fig. 3. The slower aerosol drying rate of Profile S is shown to have produced a smaller mode projected area (0.55 μm^2), and a consequently smaller mean equivalent circular diameter (1.62 μm), when compared with Profile F (mode area 0.84 μm^2, mean equivalent circular diameter 1.84 μm). Figure 4a, b shows the particle size distributions for the two temperature profiles expressed as equivalent circular diameters. The distributions are similar, except for a greater number of particles >3 μm for the faster drying rate.

Figure 5a, b shows the frequency distribution of the particle morphology, expressed as the FERET ratio. Profile S exhibited a much larger proportion of particles with a FERET ratio >0.95, i.e. close to spherical. This finding, together with a qualitative assessment of the secondary electron images, confirms that the slower drying rate reduced the incidence of non-spherical (collapsed) particles. The powders formed by slow drying did not contain the multi-indented, collapsed particles. Instead, some 'irregular' particles with one or two large perforations were present.

Figure 6a, b shows the size distribution solely for the irregular particles in each sample (Fig. 3). Irregular particles extended to considerably larger sizes (~10 μm) for Profile F. This is consistent with the expected effects of premature surface solidification, being more prevalent using faster drying rates, and inhibiting 'normal' shrinkage. Hence the multi-indented collapsed particles fall into the upper particle size fraction. The majority of the perforated particles in Profile S are mainly in the sub-4 μm size range.

Although we believe the analysis of the secondary electron images was accurate and statistically valid, it still only allowed a tiny fraction of the total sample to be analysed. Therefore, particle size analysis of bulk samples by a light scattering technique using a Malvern Mastersizer was carried out, and the results compared to the image analysis output. For both heating profiles, the Malvern size distributions contained two distinct peaks, with maxima at ~0.7 and ~3 μm (Fig. 7). However, the distributions differed in that the upper size peak (centred at ~3 μm) represented a smaller proportion of the overall sample in the more slowly dried powder (Profile S). Moreover, the maximum particles size was smaller at ~6 μm, as opposed to 9 μm for the faster heating profile. These maxima are in good agreement with the size data obtained from image analysis (Fig. 6).

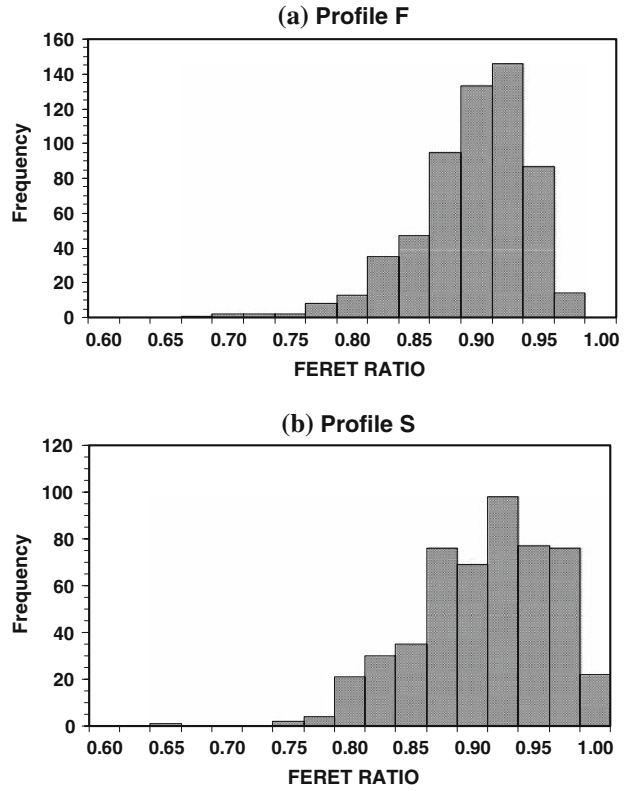

Fig. 5 Particle FERET ratio distributions for (**a**) Profile F and (**b**) Profile S

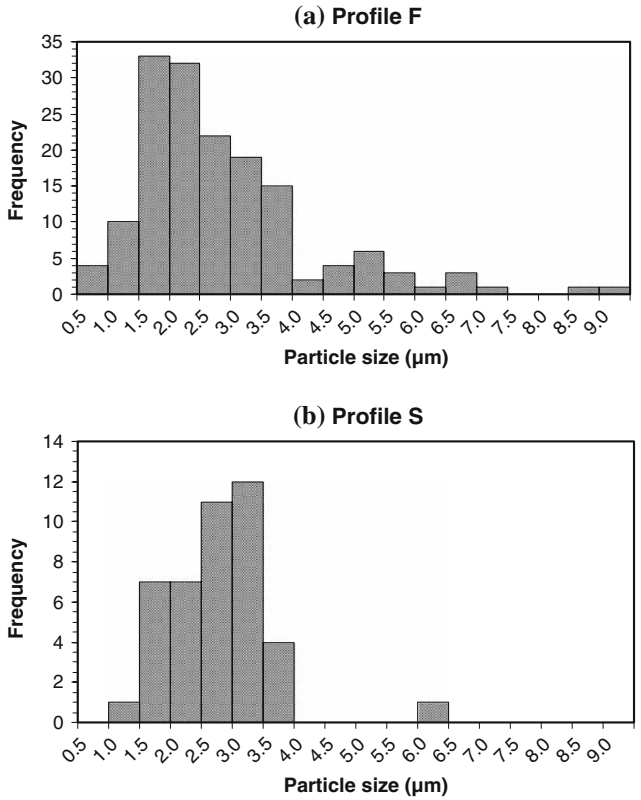

Fig. 6 Particle size distribution for the non-spherical (collapsed) particle fraction (**a**) for heating Profile F and (**b**) Profile S

Differences in the shape and the number of 'oversized' particles for each drying rate are postulated to be due to differences in the physical properties of the surface gel layer during the final stages of volatilisation. For the more slowly dried samples, it appears that the escaping gases have perforated the surface skin in one or two places but there has been very limited inward collapse of the surrounding material. This suggests that the gel skin has evolved under the slower drying to form a less-pliable coating than for rapid drying. The greater degree of collapse of the outer wall in the more rapidly dried particles suggests that the last remaining solvent escapes through a soft, pliable outer wall which can respond to the stresses generated during drying by undergoing extensive inward collapse. The possibility of diffusion of solvent through the soft surface gel layer in a non-catastrophic manner is also speculated.

Having demonstrated the effect of drying rate on particle size and shape, microtomy was employed to section embedded particles in an attempt to reveal their internal structure. For any sectioned particle it was not possible to determine whether the section passed close to the centre of the particle or was an off-centre cut, which is a potential source of misinterpretation.

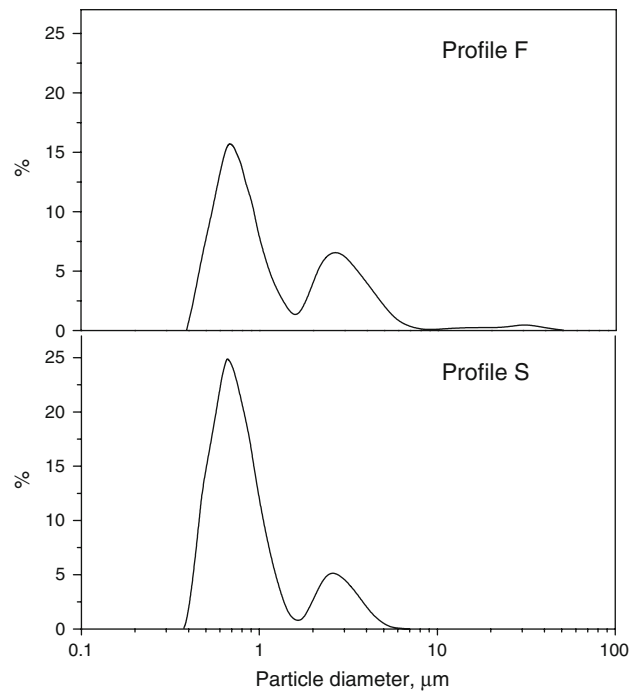

Fig. 7 Particle size data (>0.5 μm) from laser diffraction experiments for heating Profile F and Profile S

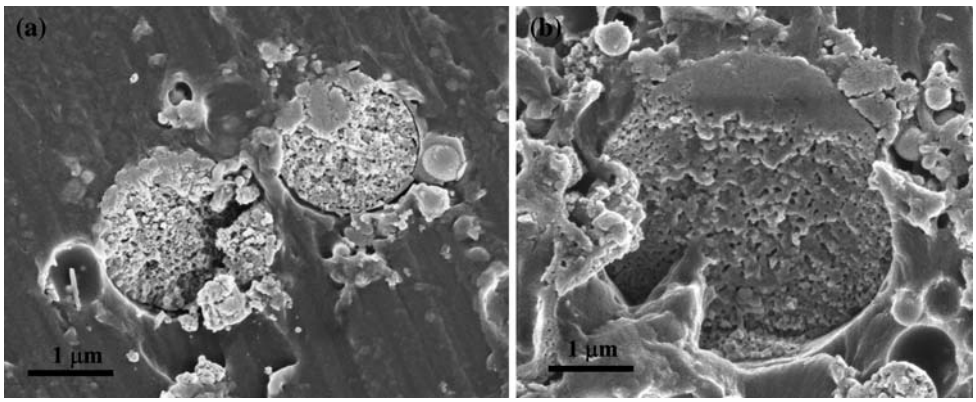

Fig. 8 Internal structure of particle (**a**) from Profile F and (**b**) from heating Profile S

Two examples of sectioned particles from a sample of Profile F are shown in Fig. 8a. The particle sections are non-hollow, but significant levels of nanoporosity are present, with pore sizes <50 nm. A similar structure is shown for a 4-μm diameter section of a Profile S particle in Fig. 8b. Given that the maximum particle size of the slowly dried sample was ~6 μm (Fig. 4b), this section is probably bisecting close to the equator of the sphere. All particles are shown to be composed of a substructure of nanoparticles a few tens of nanometre in size.

The internal structure of another type of ~3 μm particle in a Profile F sample is shown in Fig. 9. The particle is hollow with a minimum wall thickness of ~200 nm. The irregular outline of the section suggests it to originate from a collapsed particle. Figure 10a shows an example of a Profile S hollow particle with a circular wall section; it probably originates from the type of perforated spherical particle shown in normal view in Fig. 10b.

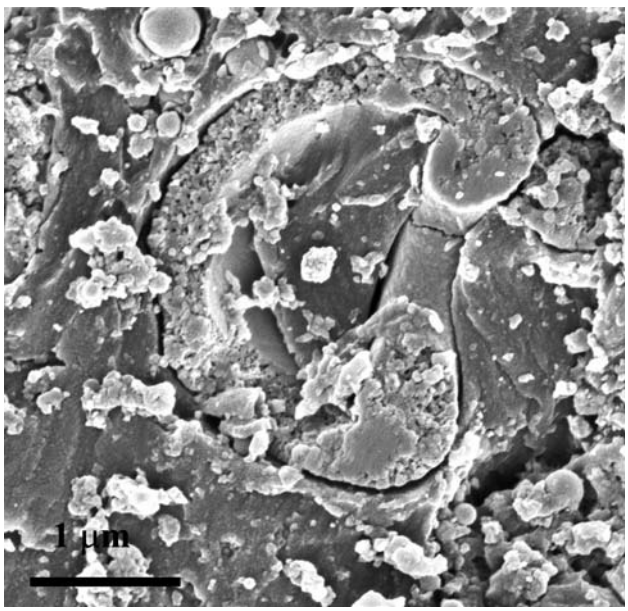

Fig. 9 Internal structure of particle from heating Profile F, showing perforation and resin infiltration

These initial findings on internal structure reveal that most of the spherical particles examined were solid throughout their structure, whilst many of the non-spherical particles were hollow, and of variable wall thickness. In terms of ceramic processing, a fraction of large hollow collapsed or hollow perforated particles in the sample is likely to be problematic for sintering to high densities. The present paper demonstrates that the frequency of hollow PZT particles can be reduced, and consequently maximum particle size decreased, through decreasing the rates at which the aerosol travels through the low-temperature section of the reactor. However, for maximum benefit, a drying rate much slower than the 160 °C s^{-1} (Profile S) permitted in the 2 m reactor used here would be required to fully eliminate the hollow particles. We suggest this could most easily be achieved by moving to a high volume, separate spray drying unit in which drying rates could be manipulated without affecting the temperatures that can be applied in the main reactor. This would permit added process flexibility for calcination and densification at high temperatures in the second reactor.

Conclusions

Reducing the heating rate in the first, sub-200 °C, section of the SP reactor altered the morphology of PZT aggregates of nanoparticles produced from sol–gel precursors, and consequently permitted a reduction in maximum particle size from ~10 to ~5 μm. Image analysis highlighted deviations from spherical aggregate morphology as well as variations in particle size. The slower heating rate produced a narrower size and shape distribution. The non-spherical fraction comprised perforated structures in place of the collapsed irregular particles which were common in powders made using the faster heating rate. Microtomy revealed that the majority of the spherical particles were

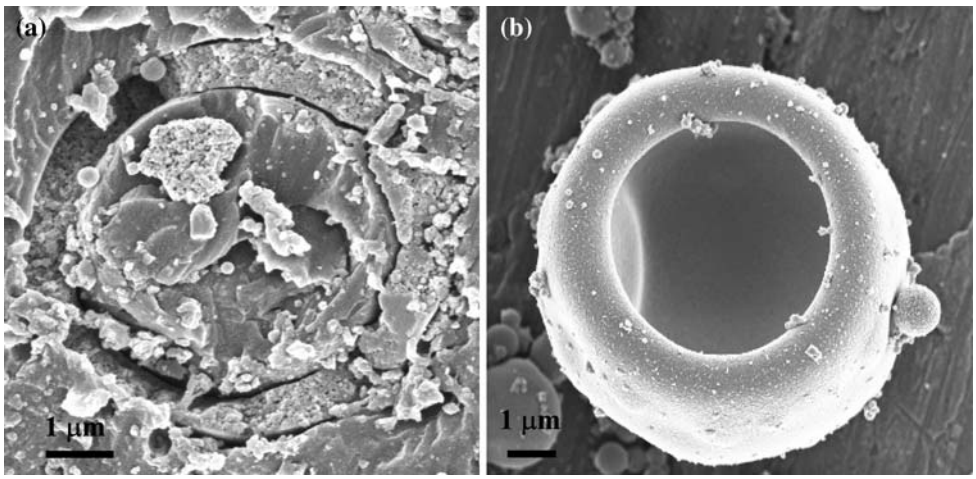

Fig. 10 High magnification view of (**a**) a microtomed non-solid particle in powders prepared using Profile S (**b**) example of non-microtomed particle revealing hollow core

solid, being composed of <100 nm primary particles, but exhibited high levels of nanoscale internal porosity. The non-spherical particle aggregates were typically hollow.

Acknowledgement The authors would like to thank the UK Engineering and Physical Sciences Research Council for financial support.

References

1. Messing GL, Zhang S-C, Jayanthi GV (1993) J Am Ceram Soc 76:2707. doi:10.1111/j.1151-2916.1993.tb04007.x
2. Ruthner MJ (1983) In: Vincenzini P (ed) Ceramic powders. Elsevier, Amsterdam, p 515
3. Milosovic B, Mirkovic MK, Uskokovic DP (1996) J Am Ceram Soc 79:1720. doi:10.1111/j.1151-2916.1996.tb08794.x
4. Janackovic D, Jokanovic V, Kostic-Gvozdenovic L, Zivkovic L, Uskokovic D (1996) J Mater Res 11:1706. doi:10.1557/JMR.1996.0214
5. Lenggoro IW, Hata T, Iskandar F, Lunden MM, Okuyama K (2000) J Mater Res 15:733. doi:10.1557/JMR.2000.0106
6. Zhang SC, Messing GL, Borden M (1990) J Am Ceram Soc 73:61. doi:10.1111/j.1151-2916.1990.tb05091.x
7. Nimmo W, Ali NJ, Brydson R, Calvert C, Hampartsoumian E, Hind D et al (2003) J Am Ceram Soc 86:1474. doi:10.1111/j.1151-2916.2003.tb03499.x
8. Nimmo W, Ali NJ, Brydson R, Calvert C, Milne SJ (2005) J Am Ceram Soc 88:839. doi:10.1111/j.1551-2916.2005.00184.x
9. Nimmo W, Hind D, Ali NJ, Hampartsoumian E, Milne SJ (2002) J Mater Sci 37:3381. doi:10.1023/A:1016549325319
10. Chin JS, Lefebvre AH (1995) J Eng Gas Turbines Power 117:266. doi:10.1115/1.2814090